

Review

Review of Smog Chamber Experiments for Secondary Organic Aerosol Formation

Hyun Kim ^{1,†}, Dahyun Kang ^{1,†}, Heon Young Jung ¹, Jongho Jeon ²  and Jae Young Lee ^{1,*} 

¹ Department of Environmental and Safety Engineering, Ajou University, 206 Worldcup-ro, Yeongtong-gu, Suwon 16499, Republic of Korea; rlagus1882@ajou.ac.kr (H.K.); erin3858@ajou.ac.kr (D.K.); jhy342@ajou.ac.kr (H.Y.J.)

² Department of Applied Chemistry, College of Engineering, Kyungpook National University, 80 Daehak-ro, Buk-gu, Daegu 41566, Republic of Korea; jeonj@knu.ac.kr

* Correspondence: jaeylee@ajou.ac.kr; Tel.: +82-31-219-2404

† These authors contributed equally to this work.

Abstract: In this study, we reviewed smog chamber systems and methodologies used in secondary organic aerosol (SOA) formation studies. Many important chambers across the world have been reviewed, including 18 American, 24 European, and 8 Asian chambers. The characteristics of the chambers (location, reactor size, wall materials, and light sources), measurement systems (popular equipment and working principles), and methodologies (SOA yield calculation and wall-loss correction) are summarized. This review discussed key experimental parameters such as surface-to-volume ratio (S/V), temperature, relative humidity, light intensity, and wall effect that influence the results of the experiment, and how the methodologies have evolved for more accurate simulation of atmospheric processes. In addition, this review identifies the sources of uncertainties in finding SOA yields that are originated from experimental systems and methodologies used in previous studies. The intensity of the installed artificial lights (photolysis rate of NO₂ varied from 0.1/min to 0.40/min), SOA density assumption (varied from 1 g/cm³ to 1.45 g/cm³), wall-loss management, and background contaminants were identified as important sources of uncertainty. The methodologies developed in previous studies to minimize those uncertainties are also discussed.

Keywords: emission; measurement system; secondary organic aerosol; smog chamber; wall loss



Citation: Kim, H.; Kang, D.; Jung, H.Y.; Jeon, J.; Lee, J.Y. Review of Smog Chamber Experiments for Secondary Organic Aerosol Formation. *Atmosphere* **2024**, *15*, 115. <https://doi.org/10.3390/atmos15010115>

Academic Editors: Rongzhi Tang and Wenfei Zhu

Received: 20 November 2023

Revised: 13 January 2024

Accepted: 15 January 2024

Published: 18 January 2024



Copyright: © 2024 by the authors. Licensee MDPI, Basel, Switzerland. This article is an open access article distributed under the terms and conditions of the Creative Commons Attribution (CC BY) license (<https://creativecommons.org/licenses/by/4.0/>).

1. Introduction

Solid and liquid aerosol particles floating in the air can originate from various sources, such as sea spraying, volcanic eruptions, industrial emissions, and fossil fuel combustion [1]. Aerosols have complex chemical structures, and their sizes vary depending on their source [2]. Aerosols larger than 2.5 μm in diameter are primarily composed of soil dust, sea salts, and plant fragments, whereas those smaller than 2.5 μm in diameter are formed in the atmosphere through fuel combustion and gas/particle conversion of volatile compounds [3]. These aerosols are important research topics because they can significantly affect visibility by scattering and absorbing solar radiation and influence climate by acting as cloud condensation nuclei [4,5]. Aerosols can also affect air quality and human health [6,7].

Organic aerosols (OAs) are the major components of atmospheric pollution and account for 20–50% of global aerosol loading [8,9]. Among OAs, primary organic aerosols are directly emitted from natural and anthropogenic sources, and secondary organic aerosols (SOAs) are formed by photochemical reactions of volatile organic compounds with oxidants. SOAs account for a significant portion of total OAs. Zhang et al. [10] showed that 64%, 83%, and 95% of total OAs at urban, urban downwind, and rural sites, respectively, were SOAs.

Because of the abundance of SOAs, many previous studies have examined their formation mechanisms and measured their production yields based on smog chamber experiments. These SOA yield data have been used in atmospheric models to forecast the total SOA mass concentrations [11]. Because the accuracy of the yield data is critical for the accurate prediction of SOA concentrations, it is very important to closely review previous SOA formation studies and understand the factors influencing the accuracy of SOA yield data.

Many previous researchers have identified key chamber parameters such as volume, surface-to-volume ratio (S/V), temperature, relative humidity, light intensity, and wall effect that influence the results of experiments, and they developed methodologies for more accurate simulation of atmospheric processes. Large chambers sized up to hundreds of cubic meters were built to reduce S/V, thereby reducing the wall loss [12–14]. EUPHORE (European Photoreactor) built in 1995 has dual 200 m³ semispherical reactors [15]. SAPHIR (Simulation of Atmospheric Photochemistry in a Large Reaction Chamber) built in 2000 has a 270 m³ cylindrical reactor [16]. HELIOS (cHambRE de simuLation atmosphérique à Irradiation naturel d’OrléanS) built in 2007 has a 90 m³ semispherical reactor [17]. These chambers were built in semispherical or cylindrical shape to reduce the surface area at a given volume [13]. In addition, researchers have improved the SOA yield calculation method by measuring aerosol density instead of using aerosol density assumptions for more accurate calculation of SOA yield [18,19]. The wall loss correction methods have also been evolved from the averaged method [20,21], where the average wall loss rate is obtained and corrected for the total aerosol concentration, to the size-dependent method [22,23], where the multiple wall loss rates for various particle sizes are calculated and corrected in order to account for the variability of wall loss depending on particle size.

This review summarizes smog chambers, measurement systems, and the methods used in previous studies on chamber-based SOA formation. The characteristics of chambers and measurement systems, as well as the underlying reasons for their widespread use in research studies, are explained. Various yield calculation and wall-loss correction methodologies developed in previous studies are summarized and compared. The characteristics of the chambers that influence the SOA simulation and the sources of uncertainties in the SOA yield data originated from the experimental systems and methodologies were identified. This review specifically focuses on chamber systems in SOA formation studies, offering a higher level of detail than that found in previous review papers on chamber-based atmospheric process studies [11–13]. The information summarized in this review will guide researchers in understanding the sources of uncertainties in SOA yield data and performing smog chamber experiments.

2. Methods

Research articles on smog chamber studies related to SOA formation, written in English, were reviewed. To search papers to review, we took two approaches. First, we listed well-known major indoor and outdoor chambers across the world, especially European chambers. Then, we found the SOA formation studies conducted in those chambers using Google Scholar and keywords such as secondary aerosol, SOA, and the name or the institute of the chambers. Second, we also searched SOA studies on Google Scholar without specifying the chambers. The following keywords were used in the search: secondary aerosol, SOA, chamber, and chamber experiment. Among numerous articles found in the search, we selected ones that provided detailed information regarding chamber specifications and experimental procedures.

In addition to reviewing the chamber studies, we identified key chamber parameters, considerations, methodologies, and source of uncertainties related to the SOA formation. The relevant studies were found either from the reference list of the reviewed chamber studies or from Google Scholar search. As a result, we reviewed 65 studies on SOA formation in total, which were published between 1978 and 2023. This study focused

on reviewing the characteristics of chambers, key considerations, methodologies, and uncertainties related to SOA formation studies.

3. Results

3.1. Chamber

Table 1 summarizes general information on the chambers used in previous studies, such as the type, reactor size, wall material, and light source of the chamber, and usage location by country and institute. Chambers can be classified as indoor, outdoor, and mobile. Indoor chambers were the dominant choice in previous chamber studies (44 out of 65) because they were designed to control input materials and meteorological conditions, such as temperature, relative humidity, and light intensity. The high level of control makes them suitable for performing experiments under diverse environmental conditions and facilitates reproducibility through multiple iterations. However, emulating the real atmosphere in indoor chamber experiments remains challenging [11].

Table 1. General information on chambers used in secondary organic aerosol studies.

Location	Country	Institute (Chamber)	Reactor Size	Wall Material	Light Source	Reference
Indoor	USA	Caltech	11.3 m ³	TFE	Fluorescent bulb	[24]
Indoor	USA	Caltech	Dual 28 m ³	FEP	Blacklight lamp	[19,25,26]
Indoor	USA	Carnegie Mellon U.	Dual 1.5 m ³	PTFE	UV lamp	[27]
Indoor	USA	Georgia Institute of Technology	Dual 12 m ³	FEP	Blacklight lamp	[23,28,29]
Indoor	USA	National Exposure Research Lab	14.5 m ³	PTFE	Fluorescent bulb	[30,31]
Indoor	USA	U. of San Diego	0.3 m ³	Tedlar/Teflon	N/A	[32]
Indoor	USA	UC Riverside	18 m ³	Teflon	Dark	[33]
Indoor	USA	UC Riverside	30 m ³	FEP	Blacklight lamp	[34]
Indoor	USA	UC Riverside	7 m ³	PTFE	Dark	[35]
Indoor	USA	UC Riverside	Dual 90 m ³	FEP	Argon arc lamp, Blacklight lamp	[20,36]
Indoor	USA	UT Austin	10 m ³	Teflon	Blacklight lamp	[37]
Indoor	USA	U. of New Hampshire	6 m ³	FEP	Blacklight lamp	[38]
Indoor	USA	Washington State U.	2 m ³	PVF	Blacklight lamp	[39]
Indoor	Germany	U. of Wuppertal (QUAREC)	1.08 m ³	Quartz	Blacklight lamp	[40]
Indoor	Germany	Institute for Energy and Climate Research	1.45 m ³	Teflon	UV lamp	[41]
Indoor	Germany	TROPOS (LEAK)	19 m ³	Teflon	Blacklight lamp	[42,43]
Indoor	Germany	KIT (AIDA)	84 m ³	Aluminium	LED	[44] *
Indoor	France	LISA (CESAM)	4.2 m ³	Stainless steel	Xenon arc lamp	[45,46]
Indoor	France	ICARE	7.3 m ³	FEP	N/A	[46]
Indoor	France	U. of the Littoral Opal Coast	8 m ³	Altuglas	Dark, Fluorescence tube	[47]
Indoor	UK	Manchester U. (MAC)	18 m ³	FEP	Xenon arc lamp	[48,49]
Indoor	UK	U. of Leeds (HIRAC)	2 m ³	Stainless steel	Blacklight lamp	[50]
Indoor	Ireland	U. College Cork (IASC)	27 m ³	FEP	UV lamp	
Indoor	Italy	INFN (CHAMBRe)	2.2 m ³	Stainless steel	UV lamp	[51] *
Indoor	Denmark	Aarhus University Research on Aerosol	5 m ³	Teflon	UV lamp	[52]
Indoor	Finland	U. of Eastern Finland (ILMARI)	29 m ³	Teflon	Blacklight lamp	[53]
Indoor	Romania	Alexandru Ioan Cuza U. (CERNESIM)	0.76 m ³	Quartz	Blacklight lamp	

Table 1. Cont.

Location	Country	Institute (Chamber)	Reactor Size	Wall Material	Light Source	Reference
Indoor	Sweden	Lund U.	6 m ³	FEP	UV lamp	[54]
Indoor	Switzerland	U. of Applied Sciences	76 mL	Quartz	Mercury lamp, UV lamp, Halogen lamp	[55]
Indoor	Switzerland	Paul Scherrer Institute (PACS)	5.5 m ³	Teflon	UV lamp	[56]
Indoor	Switzerland	Paul Scherrer Institute (PACS)	27 m ³	FEP	Xenon arc lamp	[18,57]
Indoor	China	Beijing U.	10 m ³	Quartz	Dark/UV lamp	[58]
Indoor	China	Chinese Academy of Sciences	30 m ³	FEP	Blacklight lamp	[59,60]
Indoor	China	Shandong Jianzhu U.	1 m ³	FEP	Blacklight lamp	[61]
Indoor	China	Shanghai U.	1.2 m ³	Teflon	Blacklight lamp	[62]
Indoor	China	Zhejiang U.	3 m ³	Teflon	Blacklight lamp	[63]
Indoor	Republic of Korea	Kyungpook National U.	7 m ³	FEP	UV lamp	[64]
Outdoor	USA	Caltech	60 m ³	PTFE	Sun	[65,66]
Outdoor	USA	U. of Florida (UF-APHOR)	Dual 52 m ³	FEP	Sun	[67,68]
Outdoor	USA	U. of North Carolina	190 m ³	Teflon	Dark/Sun	[69–71]
Outdoor	USA	U. of North Carolina	Dual 270 m ³	Teflon	Sun	[72,73]
Outdoor	Germany	Forschungszentrum Jülich (SAPHIR)	270 m ³	FEP	Sun	[74,75]
Outdoor	Spain	CEAM (EUPHORE)	Dual 200 m ³	Teflon	Sun	[46,76,77]
Outdoor	France	ICARE (HELIOS)	90 m ³	FEP	Sun	[17]
Outdoor	China	Chinese Research Academy of Environmental Sciences	56 m ³	FEP	Sun	[78]
Outdoor	India	Indian Institute of Technology Kanpur	12.5 m ³	FEP	Sun	[79]
Mobile	USA	Carnegie Mellon U.	7 m ³	Teflon	Blacklight lamp/Sun	[80]
Mobile	Greece	Foundation for Research and Technology Hellas (FORTH)	Dual 1.5 m ³	PTFE	UV lamp/Sun	[81,82]
Mobile	Switzerland	Paul Scherrer Institute (PACS)	9 m ³	FEP	UV lamp	[83]

* Not an SOA formation study; AIDA: Aerosol interaction and dynamics in the atmosphere; CEAM: Fundación centro de estudios ambientales del mediterráneo; CERNESIM: Integrated centre of environmental science studies in the north east region; CESAM: Chamber for experimental multiphase atmospheric simulation; CHAMBRE: Chamber for aerosol modelling and bio-aerosol research; EUPHORE: European Photoreactor; FORTH: Foundation for research and technology Hellas; HELIOS: Chambre de simulation atmosphérique à irradiation naturelle d'Orléans; HIRAC: Highly instrumented reactor for atmospheric chemistry; IASC: Irish atmospheric simulation chamber; ICARE: Institute of combustion, aerothermics, reactivity and environment; ILMARI: Aerosol physics, chemistry and toxicology research unit; INFN: Istituto nazionale di fisica nucleare; KIT: Karlsruhe institute of technology; LEAK: Leipziger aerosolkammer; LISA: Laboratoire interuniversitaire des systèmes atmosphériques; MAC: Manchester aerosol chamber; PACS: Paul Scherrer institute atmospheric simulation chambers; QUAREC: Quartz reactor; SAPHIR: Simulation of atmospheric photochemistry in a large reaction chamber; TROPOS: Leibniz institute for tropospheric research; UF-APHOR: University of Florida—The atmospheric photochemical outdoor reactor.

Overall, 17 of the 65 studies used outdoor chambers, which are normally installed on the rooftops and terraces of buildings. Outdoor chambers allow input material control but have limited controllability against meteorological conditions because they are typically exposed directly to outdoor conditions such as temperature and sunlight. Ambient air [69], purified air [78], or their mixture [72,73] is used as the background air of experiments. Relative humidity can be controlled even in outdoor chambers using dry purified air or humidifiers [65,72]. The advantage of outdoor chambers is that the experiments are conducted under conditions similar to those of the real atmosphere, thereby limiting controllability and reproducibility. Behera and Sharma [79] selected an outdoor chamber using sunlight and claimed that artificial light sources do not have the same spectrum as that of sunlight. Zhou et al. [73] used outdoor chambers to investigate the effects of humidity on

aerosol formation under real atmospheric conditions. The last type of chamber is a mobile chamber that can be moved and installed in any place, including indoors, outdoors, and in vehicles such as cars and airplanes. Miracolo et al. [80] used a mobile chamber in an airplane to investigate the effect of airplane exhaust on SOA formation, and Platt et al. [83] used a mobile chamber to study SOA formation from gasoline vehicle emissions.

The reactor size (part of the chamber where the reactions were conducted) used in previous studies varied from 76 mL to 270 m³. Typically, outdoor chambers (12.5 to 270 m³) were larger than indoor chambers (76 mL to 90 m³). Large chambers are preferred to minimize the effect of wall loss (see Section 3.7 for more details) because they could have a small surface-area-to-volume ratio. However, cleaning, mixing, and conducting reaction studies in large volumes of large chambers can be time-consuming [84]. Eight chambers have dual reactors, in which one reactor can serve as the experimental chamber while the other can serve as the control chamber [27]. This allows for an examination of the effects of a parameter that was designed to be different in the two reactors. This characteristic is essential for outdoor chambers to overcome the difficulty in recreating weather conditions.

The chamber walls were typically fabricated using fluoropolymers, such as polytetrafluoroethylene (PTFE), fluorinated ethylene propylene (FEP), tetrafluoroethylene (TFE), and polyvinyl fluoride (PVF). These polymers have outstanding chemical, thermal, and ultraviolet (UV) resistance, making them suitable as reactor wall materials. PTFE is mechanically stable [85] and has excellent abrasion resistance [86], electrical stability, low coefficient of friction, and low dielectric constant [87]. FEP is more transparent than the other materials and is desirable for delivering external light inside a chamber for photochemical reaction experiments. Paulsen et al. [57] showed that FEP transmits >90% light in the 290–800 nm wavelength range, whereas PVF has a high UV light filtration capacity. Other than fluoropolymers, quartz, stainless steel, and aluminium were used as wall materials. Quartz is also known for its chemical resistance and high UV transmittance. Among 65 previous studies, only four chambers used quartz as the chamber wall material. Table 1 summarizes the wall materials used in previous studies. The brand names Teflon, Tedlar, and Altuglas were listed rather than the actual material names in some previous studies, because the material name was not specified in the manuscripts.

3.2. Experimental Method and Procedure

The majority of previous chamber-based studies followed a typical experimental method and procedure explained in this section. Prior to SOA experiment, researchers performed characterization of lighting, background contaminants, and wall effect [20]. They also calibrated measurement devices based on synthetic standard samples. For an accurate simulation of SOA formation processes, chambers were flushed for several hours with background air (purified or ambient air) to remove any unwanted contaminants previously captured inside the chamber system. Pure air generators or filters were used to supply purified air. Carter et al. (2005) [20] used a pure air generator (Aadco 737, Cleves, OH, USA) and achieved background concentrations of particles <0.2 cm⁻³, non-methane hydrocarbons < 1 ppb, and NO_x < 10 ppt. Babar et al. (2016) [64] used activated carbon beds and HEPA filters to purify ambient air to achieve background concentrations of particles < 10 cm⁻³, VOCs (C5–C10) < 1 ppb, NO_x < 1 ppb, and O₃ < 1 ppb. Unlike these two studies, there are also many chamber studies, which used unpurified ambient air in order to simulate SOA formation under real atmospheric environment. Instead of removing contaminants, these studies typically reported the characterization of background contaminants [69–71,73,77,79]. Temperature and relative humidity were set to the target and maintained to reach steady-state conditions. After the cleaning and initialization of the chamber, pollutants (parent hydrocarbon, oxidants, and other gaseous pollutants) were injected and their concentrations were monitored throughout the experiment. The gaseous and particulate product of the reaction were identified and measured using a measurement system connected to the outlet of the chamber. The amount of generated SOA was corrected

for the wall loss. In-depth discussions related to light, temperature, humidity, measurement system, SOA calculation, and wall loss can be found in Sections 3.3–3.7.

3.3. Light Sources

Light affects oxidation reactions and plays an important role in the formation of SOAs. For example, Bejan et al. (2020) showed that the photolysis of nitrophenols is an importance source of SOA [40]. Therefore, most previous studies have used artificial or natural light to simulate atmospheric photooxidation inside the chamber. Most indoor chambers are equipped with gas-discharge lamps, such as fluorescent bulbs, blacklight lamps, UV lamps, argon arc lamps, and xenon arc lamps, as artificial light sources, whereas outdoor chambers are designed to receive sunlight (Table 1). The mobile chamber used by Miracolo et al. [80] uses either black light or sunlight, and the mobile chamber used by Kaltsonoudis et al. [81] uses either UV lamps or sunlight.

One of the primary considerations in selecting artificial light sources is the similarity of their spectral distribution to that of sunlight. Xenon and Argon arc lamps offer closely comparable simulations of sunlight within the UV and visible spectral ranges [18,20]. However, blacklight lamps primarily emit UV light, with very little visible light. Therefore, the photolysis rates of O₃ and NO₃, which are affected by long wavelengths of light, are significantly reduced by blacklight [20].

The intensity of light is also very important parameter in SOA formation, since it affects the formation rate. The intensity is determined by many factors such as the number of light bulbs, installation location, and spectral characteristics of each lamp. The light bulbs were typically installed on the inner surface of the exterior enclosure [20,34,58,59], and tens of centimeters away from the reactor wall to prevent from overheating the reactor surface [61,64].

The aggregated characteristics of the set of lights must be empirically determined based on the measurement of the spectral distribution using spectroradiometer or chemical actinometry experiments such as NO₂ photolysis. The spectral distribution or photolysis rate measured inside the chamber must be similar to those of sunlight for an accurate simulation of atmospheric process. Table 2 summarizes the information on the intensity and spectral characteristics of artificial lights used in previous studies. Sixteen previous studies reported the photolysis rate of NO₂, which ranged from 0.1/min to 0.40/min. Only two studies provided the full spectral distribution of their light sources with respect to that of sunlight [20,64]. Carter et al. (2005) [20] showed how the spectrum of argon arc light resembled that of sunlight between wavelengths of 300 nm and 600 nm (Figure 2 of [20]). Babar et al. (2016) [64] compared the spectral distributions of the UV lamp and sunlight between wavelengths of 200 nm and 600 nm (Figure 6 of [64]). Twenty studies provided information on the peak wavelengths of their lights instead of the full spectrum.

Table 2. Intensity and spectrum of artificial light sources.

First Author	Year	Light Intensity	Light Spectrum	Ref.
Al-Naiema	2020	NO ₂ photolysis rate (0.34/min)	Peak wavelength (300–400 nm)	[31]
Babar	2016	NO ₂ photolysis rate (0.17/min)	Full spectral distribution	[64]
Bejan	2020	-	Peak wavelength (360 nm)	[40]
Boyd	2015	NO ₂ photolysis rate (0.28/min)	Peak wavelength (354 nm)	[28]
Cai	2008	-	Peak wavelength (365 nm)	[38]
Carter	2005	NO ₂ photolysis rate (0.26/min)	Full spectral distribution	[20]
Chen	2020	NO ₂ photolysis rate (0.38/min)	-	[63]
Deng	2020	NO ₂ photolysis rate (0.25/min)	-	[60]
Du	2022	NO ₂ photolysis rate (0.11~0.18/min)	-	[48]
Hartikainen	2018	-	Peak wavelength (350 nm)	[53]
Jahn	2021	-	Peak wavelength (354 nm)	[37]
Kaltsonoudis	2019	NO ₂ photolysis rate (0.1/min)	Peak wavelength (350–400 nm)	[81]

Table 2. Cont.

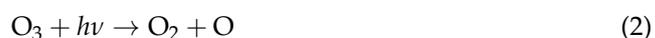
First Author	Year	Light Intensity	Light Spectrum	Ref.
Keller	2012	-	Peak wavelength (254 nm)	[55]
Kleindienst	2007	-	Peak wavelength (300–400 nm)	[30]
Kristensen	2020	NO ₂ photolysis rate (0.2/min)	Peak wavelength (350 nm)	[52]
Lee	2006	-	Peak wavelength (354 nm)	[25]
Ma	2022	NO ₂ photolysis rate (0.40/min)	Peak wavelength (371 nm)	[58]
Murphy	2007	-	Peak wavelength (354 nm)	[26]
Nordin	2013	NO ₂ photolysis rate (0.2/min)	Peak wavelength (350 nm)	[54]
Paulsen	2005	NO ₂ photolysis rate (0.12/min)	Note 1	[57]
Platt	2013	NO ₂ photolysis rate 0.24 /min	Peak wavelength (368 nm)	[83]
Pullinen	2020	-	Peak wavelength (365 nm)	[41]
Qi	2020	NO ₂ photolysis rate (0.17/min)	Peak wavelength (365 nm)	[62]
Schuetzle	1978	Note 2	-	[39]
Seinfeld	2003	-	Peak wavelength (244 nm)	[24]
Stefenelli	2019	-	Peak wavelength (400 nm)	[56]
Vu	2019	NO ₂ photolysis rate (0.23/min)	Peak wavelength (365 nm)	[34]
Wang	2021	NO ₂ photolysis rate (0.117/min)	-	[61]

Note 1. Authors claimed that Xenon arc lamp has a spectral density similar to that of sunlight. Note 2. Authors claimed that the light intensity corresponds to 75% of noontime sunlight.

3.4. Temperature and Humidity

Temperature is one of the important parameters in SOA formation, since high temperature increases the vapor pressure of VOCs. As a result, heat typically has a negative effect on SOA formation, as shown in many previous studies. Kristensen et al. [52] claimed that the SOA formed from α -pinene under the presence of ozone increased due to increased condensation of semivolatile oxidation products at lower temperature, and Von Hessberg et al. [88] showed that SOA yield from ozonolysis of β -pinene increased as the temperature decreased under dry condition.

Humidity is another important parameter in SOA formation, since it affects the proton transfer and oxidation processes in SOA formation. Previous studies have identified how the water vapor intervenes the partitioning of key precursors and oxidants, which in turn may positively and negatively affect the yield of SOA formation. For example, nitrogen dioxide (NO₂) reacts with water vapor (hydrolysis) to form nitrous acid (HONO) and nitric acid (HNO₃) [89]. Ozone photolysis in the presence of water vapor forms hydroxyl radical (OH) [90]. These reactions can be formulated as below.



In addition, humidity perturbs the thermodynamic equilibrium between gas- and particle-phase organics. As a result, gas-phase organic mass may condense into wet seed particles, increasing the yield of SOA formation [91,92]. Seinfeld et al. (2001) [92] showed that the SOA yield increases with increased relative humidity in α -pinene-, β -pinene-, sabinene-, Δ^3 -carene-, and cyclohexene-ozone systems.

Due to their important roles, accurate measurement of temperature and humidity is critical in an atmospheric simulation chamber. A temperature measurement device can be a thermocouple, resistant sensor, ultrasonic anemometer, or fiber optic sensor, and it must be selected based on the consideration of the measurement range, precision, and time resolution [93]. For example, fast sensors with low heat capacities may not be suitable for simulation with condensable compounds due to latent heat transfer. In addition, the temperature sensor needs to be covered to prevent direct exposure to light radiation [20]. Humidity can be measured using thin-film capacitive humidity sensors or dew point mirror sensors [93]. The capacitive sensors measure the humidity-induced change in dielectric

constant between a pair of electrodes. Researchers need to be careful in using the capacitive sensors in an experiment with high concentrations of oxidizing reactants, since they may destroy the sensors. Dew point mirror sensors measure the dew point temperature based on the light reflection caused by condensed water on the mirror. This type of sensor is suitable when the major condensing species in the chamber is water [93].

The ability to control temperature and humidity is also important to simulate SOA formation under a wide range of temperature and humidity. For indoor chambers, temperature is controlled by an air conditioning system installed inside the enclosure. For outdoor chambers, the reactors are directly exposed to outdoor temperature, however temperature can still be controlled by cooling the floor of the reactor [12]. Relative humidity can be controlled in both indoor and outdoor chambers using purified air and humidifiers which are connected to the inlet of the reactors.

Table 3 summarized the temperature and humidity conditions used in previous chamber studies. Most experiments were conducted under room temperature (between 20 and 30 °C) and dry condition (relative humidity of <10%). As can be seen in Table 3, there were a few studies that used multiple temperature and humidity conditions to assess the effects of temperature and humidity on SOA formation. Kristensen et al. [52] used a subzero temperature and showed that the α -pinene ozonolysis rate increased significantly at low temperatures. Jahn et al. [37] conducted a chamber simulation under both dry and humid conditions and showed higher SOA yields for decane without any oxidants at the humid condition, whereas Na et al. [33] showed that a high humidity condition has a negative effect on the SOA formation from styrene ozonolysis.

Table 3. Temperature and humidity conditions of chamber experiments.

Location	First Author	Year	Temperature	Humidity	Ref.
Indoor	Al-Naiema	2020	-	30%	[31]
	Babar	2016	24 °C	<3%	[64]
	Bahreini	2005	20 ± 2 °C	<10%, 55 ± 5%	[19]
	Bejan	2020	10–40 °C	-	[40]
	Boyd	2015	-	<2%, 50%, 70%	[28]
	Cai	2008	24–27 °C	-	[38]
	Carter	2005	27–32 °C	-	[20]
	Chen	2020	37 °C	7%, 63–68%	[63]
	Deng	2017	24.6–26.9 °C	50.5–63.7%	[59]
	Deng	2020	25 ± 1 °C	2.7–10.3%	[60]
	Du	2022	25 °C	50%	[48]
	Docherty	2005	25 ± 3 °C	<0.5%	[35]
	Fisseha	2004	20 °C	40–50%	[18]
	Gatzsche	2017	-	<55%	[43]
	Hastings	2005	20 °C	22–44%	[32]
	Hartikainen	2018	18 ± 2 °C	60 ± 5%	[53]
	Henry	2008	21 ± 2 °C	6–10%	[47]
	Jahn	2021	-	<5%, 40–55%	[37]
	Jorga	2020	23–25 °C	20–70%	[27]
	Keller	2012	25–35 °C	<4%, 21–24%	[55]
	Kristensen	2020	−14.5–20.3 °C	0–19.8%	[52]
	Lamkaddam	2017	50 °C	<1%	[45]
	Lee	2006	20–22 °C	40–56%	[25]
	Ma	2022	15–30 ± 1 °C	<10%	[58]
	Murphy	2007	20–25 °C	<10%	[26]
	Na	2006	20 ± 1 °C	<2%, 50–60%	[33]
Nah	2016	25 °C	<5%	[23]	
Nah	2017	25 °C	<5%	[29]	
Nordin	2013	22 ± 2 °C	3–10%	[54]	
Paulsen	2005	23.5 ± 1 °C	50%	[57]	

Table 3. Cont.

Location	First Author	Year	Temperature	Humidity	Ref.
Indoor	Qi	2020	25 ± 2 °C	<20%	[62]
	Song	2005	27 °C	<2%	[36]
	Stefenelli	2019	−10, 2, 15 °C	50%	[56]
	Vu	2019	25, 30 °C	<7%	[34]
	Wang	2021	25 ± 3 °C	29 ± 3%	[61]
	Wang	2022	25 ± 2 °C	50 ± 5%	[49]
Outdoor	Behera	2011	35.8 ± 5.7 °C	58.3 ± 17.5%	[79]
	Couvidat	2018	21–36 °C	0.4–37%	[77]
	Jang	1999	−5–24 °C	55–100%	[70]
	Jang	2001	29–31 °C	34–38%	[71]
	Kamens	1999	6–23 °C	55–100%	[69]
	Leungsakul	2005	8–40 °C	-	[72]
	Li	2021	2–44 °C	<1%	[78]
	Madhu	2023	4–52 °C	12–99%	[68]
Mobile	Zhou	2011	2–40 °C	9–98%	[73]
	Jorga	2021	13–24 °C	30–45%	[82]
	Miracolo	2011	23 ± 2.5 °C	14.7 ± 3.8%	[80]
	Platt	2013	22 °C	-	[83]

3.5. Measurement Systems

Tables 4 and 5 summarize the detection devices used in SOA studies. These devices can be classified as general pollutant detectors, which can be used to detect a wide range of pollutants, or as specific pollutant detectors, which can be used to detect specific pollutants.

Table 4. Commonly used detection equipment in secondary organic aerosol studies.

Category	Pollutant	Basis for Detection	Equipment	Typical Result
General pollutant detector	Gas	Surface affinity (SA)	GC-ECD GC-FID GC-PID	Nitrate concentration Hydrocarbon concentration Hydrocarbon concentration
		Mass	ESI-MS, LDI-MS, MS, PTR-MS, SPI-MS, CI-MS	Mass spectrum of gas-phase oxidation product
		SA and mass	GC-MS, GC-MSD	Mass spectrum of gas-phase oxidation product
	Ion	Ion affinity	IC, PILS-IC	Ion concentration
		Ion affinity and mass	IC-MS	Mass spectrum of ion oxidation product
	Particle	N/A	CPC	Count of SOA
Size		EAA, SEMS (DMA-CPC), SMPS (DMA-CPC)	Size spectrum of SOA	
Mass		AMS	Mass spectrum of SOA	
Size and mass		APM-SMPS	Density spectrum of SOA	
	Light absorption	FTIR	Infrared absorption spectrum of SOA	

Table 4. Cont.

Category	Pollutant	Basis for Detection	Equipment	Typical Result
Specific pollutant detector	NO _x	-	NO _x analyzer	NO _x concentration
	O ₃	-	O ₃ analyzer	O ₃ concentration
	CO, CO ₂	-	CO, CO ₂ analyzer	CO, CO ₂ concentration
	SO ₂	-	SO ₂ analyzer	SO ₂ concentration
	NH ₃	-	NH ₃ analyzer	NH ₃ concentration

AMS: Aerosol mass spectrometer; APM-SMPS: Aerosol particle mass analyzer-scanning mobility particle sizer; CI-MS: Chemical ionization-mass spectrometer; CPC: Condensation particle counters; DMA: Differential mobility analyzer; EAA: Electrical aerosol analyzer; ESI-MS: Electrospray ionization-mass spectrometry; FTIR: Fourier-transform infrared; GC-ECD: Gas chromatograph-electron capture detector; GC-FID: Gas chromatograph-flame ionization detector; GC-MS: Gas chromatography-mass spectrometry; GC-MSD: Gas chromatograph-mass selective detector; GC-PID: Gas chromatograph-photoionization detector; IC: Ion chromatography; IC-MS: Ion chromatography-mass spectrometry; LDI-MS: Laser desorption ionization-mass spectrometry; MS: Mass spectrometry; PILS-IC: Particle into liquid sampler-ion chromatography; PTR-MS: Proton transfer reaction-mass spectrometry; SEMS: Scanning electrical mobility spectrometer; SMPS: Scanning mobility particle sizer; SPI-MS: Single photon ionization-mass spectrometry.

Table 5. General pollutant detectors used in previous secondary organic aerosol studies.

First Author	Year	Gas			Ion		Particle			Ref.	
		Detector	MS	Hybrid	Detector	Hybrid	Sizer	MS	Hybrid		FTIR
Al-Naiema	2020	GC-FID			IC						[31]
Babar	2016	GC-PID					SMPS				[64]
Bahreini	2005	GC-FID					SEMS	AMS			[19]
Behera	2011									FTIR	[79]
Bejan	2020						SMPS				[40]
Boyd	2015	GC-FID	CI-MS				SMPS	AMS			[28]
Brownwood	2021		CI-MS				SMPS	AMS			[75]
Cai	2008	GC-FID					SMPS	AMS			[38]
Carter	2005	GC-FID					SEMS				[20]
Couvidat	2018						SMPS				[77]
Chen	2020			GC-MS			SMPS	AMS			[63]
Deng	2017	GC-FID	PTR-MS	GC-MS			SMPS	AMS			[59]
Deng	2020	GC-FID	PTR-MS	GC-MS			SMPS	AMS			[60]
Du	2022		CI-MS								[48]
Docherty	2005	GC-FID					SMPS	AMS			[35]
Emanuelsson	2013		PTR-MS				SMPS				[74]
Fisseha	2004		PTR-MS	GC-MS		IC-MS	SMPS	AMS			[18]
Gatzsche	2017		PTR-MS				SMPS				[43]
Hastings	2005		ESI-MS	GC-MS			SMPS				[32]
Hartikainen	2018		PTR-MS	GC-MS			SMPS	AMS			[53]
Henry	2008	GC-FID					SMPS				[47]
Jahn	2021		CI-MS				SEMS				[37]
Jang	1999			GC-MS						FTIR	[70]
Jang	2001			GC-MS						FTIR	[71]
Jorga	2020		PTR-MS				SMPS	AMS			[27]
Jorga	2021		PTR-MS				SMPS	AMS			[82]
Kaltsonoudis	2019		PTR-MS				SMPS	AMS			[81]
Kamens	1999	GC-FID					EAA				[69]
Keller	2012						SMPS				[55]
Kleindienst	2007			GC-MS							[30]
Kristensen	2020	GC-FID	PTR-MS				SMPS				[52]
Lamkaddam	2017		PTR-MS				SMPS			FTIR	[45]
Lee	2006	GC-FID	PTR-MS								[25]
Leungsakul	2005	GC-ECD					SMPS			FTIR	[72]

Table 5. Cont.

First Author	Year	Gas			Ion		Particle			Ref.	
		Detector	MS	Hybrid	Detector	Hybrid	Sizer	MS	Hybrid		FTIR
Li	2021			GC-MS			SMPS			FTIR	[78]
Ma	2022		SPI-MS, PTR-MS				SMPS				[58]
Madhu	2023	GC-FID			PILS-IC		SMPS				[68]
Miracolo	2011			GC-MS			SMPS	AMS			[80]
Murphy	2007		LDI-MS		PILS-IC		DMA	AMS			[26]
Na	2006	GC-FID					SEMS				[33]
Nah	2016	GC-FID					SMPS	AMS			[23]
Nah	2017	GC-FID					SMPS	AMS			[29]
Nordin	2013		PTR-MS	GC-MS			SMPS	AMS			[54]
Odum	1997	GC *					SEMS				[66]
Pandis	1991	GC-FID		GC-MS			SEMS				[65]
Paulsen	2005	GC-FID	LDI-MS, PTR-MS	GC-MS	IC	IC-MS	SMPS			FTIR	[57]
Platt	2013						SMPS			FTIR	[83]
Pullinen	2020		PTR-MS	GC-MS				AMS			[41]
Qi	2020		SPI-MS				SMPS	AMS			[62]
Schuetzle	1978		MS								[39]
Seinfeld	2003	GC-FID					SMPS				[24]
Song	2005	GC-FID					SMPS				[36]
Stefenelli	2019		PTR-MS	GC-MS			SMPS	AMS			[56]
Vu	2019						SMPS	AMS	APM- SMPS		[34]
Wang	2021	GC-FID		GC-MS			SMPS				[61]
Wang	2022							AMS			[49]
Yu	2021	GC-FID			PILS-IC		SMPS			FTIR	[67]
Zhou	2011						SMPS				[73]

* Detector unspecified; AMS: Aerosol mass spectrometer; APM-SMPS: Aerosol particle mass analyzer-scanning mobility particle sizer; CI-MS: Chemical ionization-mass spectrometry; CPC: Condensation particle counters; DMA: Differential mobility analyzer; EAA: Electrical aerosol analyzer; ESI-MS: Electrospray ionization-mass spectrometry; FTIR: Fourier-transform infrared; GC: Gas chromatograph; GC-ECD: Gas chromatograph-electron capture detector; GC-FID: Gas chromatograph-flame ionization detector; GC-PID: Gas chromatograph-photoionization detector; GC-MS: Gas chromatography-mass spectrometry; GC-MSD: Gas chromatograph-mass selective detector; IC: Ion chromatography; IC-MS: Ion chromatography-mass spectrometry; LDI-MS: Laser desorption ionization-mass spectrometry; MS: Mass spectrometry; PILS-IC: Particle into liquid sampler-ion chromatography; PTR-MS: Proton transfer reaction-mass spectrometry; SEMS: Scanning electrical mobility spectrometer; SMPS: Scanning mobility particle sizer.

Generally, pollutant detectors are equipped with an apparatus that separates monodisperse pollutants from mixtures. The most popular separation method used in SOA studies for gaseous pollutants is gas chromatography (GC), which separates gases based on their affinity with the GC column material, while the gas mixture passes through a long and thin GC column. The separated monodisperse gas exiting a GC is commonly detected using a flame ionization detector (FID), which measures the number of ions formed during the combustion of the gas in the FID flame (22 studies used GC-FID, see Table 5). This equipment provides reliable concentration measurements with a wide dynamic range for hydrocarbon measurements. An electron capture detector (ECD) and a photoionization detector (PID) can also be used in SOA studies because the ECD is effective in detecting nitrates, and the PID is effective in detecting both organic and inorganic compounds that can be ionized by ultraviolet light. Detectors that effectively detect the chemicals of interest have been chosen in previous studies. The majority of previous studies used GC-FID to detect reactive organic gases (ROGs). Leungsakul et al. (2005) [72] used GC-ECD to detect peroxyacetyl nitrate (PAN), as a reaction byproduct of d-limonene in the presence of NO and NO₂. Babar et al. (2016) [64] used GC-PID to detect ROGs such as α -pinene, d-limonene, isoprene, toluene, benzene, ethyl benzene, styrene, and 1,3,5-trimethylbenzene.

Another technique commonly used in SOA studies is mass spectrometry (MS), which separates pollutants by mass and produces a mass spectrum (mass versus abundance). In the majority of SOA studies (34 out of 65 studies), MS has been used to identify gas-phase oxidation products and measure their concentrations. Gas chromatography-MS (GC-MS), also known as gas chromatography-mass selective detector (GC-MSD), is the most widely used technique (used in 17 studies), which first separates gas mixtures into monodisperse gases using GC and then detects their mass spectra using MS. This configuration makes the interpretation of the mass spectrum much easier (because the spectrum is generated from a monodisperse gas) and allows isomers to be distinguished. However, GC-MS measurements cannot be performed in real-time. Proton transfer reaction-MS (PTR-MS) is another type of MS that is widely used in SOA studies (17 studies). It is based on a proton transfer reaction mechanism that ionizes the sample gas and offers soft ionization, which causes less molecular fragmentation [25,57]. Because of soft ionization, it can be used without GC, which makes continuous measurement of the mass spectrum possible. Other MS devices, such as those with electrospray ionization, laser desorption ionization, single photon ionization, and chemical ionization, have been used only in a few previous studies.

The measurement of SOA, a particle-phase oxidation product, is also critical for SOA research. For this purpose, a scanning mobility particle sizer (SMPS) (also known as a scanning electrical mobility spectrometer (SEMS)) is the most widely used device in SOA studies (46 out of 65 studies). This uses a combination of a differential mobility analyzer (DMA) for size-based particle separation and a condensation particle counter (CPC) for particle counts to measure the size distribution of SOAs [94]. Aerosol mass spectrometer (AMS) is also widely used (23 out of 65 studies) to identify SOAs based on their mass profiles. Other devices, such as an electrical aerosol analyzer (EAA), which detects the size distribution of particles, and an aerosol particle mass analyzer (APM), which separates polydisperse particles into monodisperse particles by mass, have also been used in previous studies. Vu et al. [34] used APM before SMPS to detect the density distribution of SOAs. Fourier-transform infrared (FTIR) is another popular equipment used in previous studies (9 out of 65 studies) to identify ROG or the oxidation product of their experiments [71,72]. FTIR measures the amount of light absorbed by a sample for various frequencies of infrared radiation. Since different functional groups absorb different frequencies of infrared radiation, we can identify ROG or the oxidation product by comparing the FTIR spectra of a sample with the spectra of synthetic standards [57].

In conjunction with the general pollutant detectors explained above, many previous SOA studies have used specific pollutant detectors to measure the concentrations of oxidants, such as NO_x , O_3 , CO , CO_2 , SO_2 , and NH_3 . These were the key factors influencing the rate of SOA formation; thus, they were monitored throughout the experiment.

3.6. SOA Yield

Estimating SOA yield under various formation mechanisms is one of the main purposes of chamber-based SOA studies. The yield is defined as follows [66]:

$$Y = \frac{\Delta M_0}{\Delta \text{ROG}} \times 100 \quad (4)$$

where ΔM_0 is the total mass concentration of secondary organic aerosol produced, usually in $\mu\text{g}/\text{m}^3$, and ΔROG is the mass concentration of reacted organic gas (ROG).

The mass concentration of the gas-phase parent hydrocarbon (or ΔROG) is most commonly measured using GC-FID (see Table 5). The mass concentration of formed SOA (or ΔM_0) was calculated based on the particle size measured using SMPS or SEMS (assuming the particle to be spherical), as well as the density information to convert the size into mass. Table 6 summarizes the density information used in previous SOA studies. Some studies assumed the density to be $1 \text{ g}/\text{cm}^3$ (10 studies, see Table 6), $1.2 \text{ g}/\text{cm}^3$ [68], $1.25 \text{ g}/\text{cm}^3$ [25], $1.35 \text{ g}/\text{cm}^3$ [63], $1.4 \text{ g}/\text{cm}^3$ (eight studies, see Table 6), or $1.3\text{--}1.45 \text{ g}/\text{cm}^3$ [58], whereas some other studies calculated the aerosol density using a combination of a particle sizer and

an AMS [18,19,23,26,27,29,43,67,80]. Note that the density of SOA measured by Bahreini et al. [19] largely varied according to the parent hydrocarbon from 0.64 g/cm³ (linalool) to 1.45 g/cm³ (cyclohexene).

Table 6. Aerosol density for secondary organic aerosol yield calculation.

First Author	Year	Density for SOA Yield Calculation	Ref.
Babar	2016	1 g/cm ³ (assumed)	[64]
Bahreini	2005	0.64–1.45 g/cm ³ (measured)	[19]
Cai	2008	1 g/cm ³ (assumed)	[38]
Chen	2020	1.35 g/cm ³ (assumed)	[63]
Deng	2017	1.4 g/cm ³ (assumed)	[59]
Deng	2020	1 g/cm ³ (assumed)	[60]
Docherty	2005	1 g/cm ³ (assumed)	[35]
Emanuelsson	2013	1.4 g/m ³ (assumed)	[74]
Fisseha	2004	1.38 g/m ³ (measured)	[18]
Gatzsche	2017	1 g/cm ³ (measured)	[43]
Henry	2008	1.4 g/cm ³ (assumed)	[47]
Jorga	2020	1.25–1.35 g/cm ³ (measured)	[27]
Kristensen	2020	1.4 g/m ³ (assumed)	[52]
Lee	2006	1.25 g/cm ³ (assumed)	[25]
Leungsakul	2005	1 g/cm ³ (assumed)	[72]
Ma	2022	1.3–1.45 g/cm ³ (assumed)	[58]
Madhu	2023	1.2 g/cm ³ (assumed)	[68]
Miracolo	2011	1.1 g/m ³ (measured)	[80]
Murphy	2007	1–1.1 g/cm ³ (measured)	[26]
Na	2006	1 g/cm ³ (assumed)	[33]
Nah	2016	1.37–1.39 g/cm ³ (measured)	[23]
Nah	2017	1.37 g/cm ³ (measured)	[29]
Odum	1997	1 g/cm ³ (assumed)	[66]
Pandis	1991	1.4 g/cm ³ (assumed)	[65]
Paulsen	2005	1 g/cm ³ (assumed)	[57]
Qi	2020	1.4 g/cm ³ (assumed)	[62]
Song	2005	1 g/cm ³ (assumed)	[36]
Wang	2021	1.4 g/cm ³ (assumed)	[61]
Wang	2022	1.4 g/cm ³ (assumed)	[49]
Yu	2021	1.38 g/cm ³ (measured)	[67]
Zhou	2011	1 g/cm ³ (assumed)	[73]

The aerosol density (ρ_p) can be measured using SMPS and an AMS based on the following equation [24,26,95,96], assuming the simple case of spherical particle without voids.

$$\rho_p = \frac{d_{va}}{d_m} \quad (5)$$

Here, d_{va} is the vacuum aerodynamic diameter measured by AMS, and d_m is the electrical mobility diameter measured by SMPS. A more generalized equation that can be applied for various particle types can be found in [24,26,95,96].

The APM-SMPS used by Vu et al. [34] can also provide direct measurement of the aerosol density, as follows [96].

$$\rho_p = \frac{m_p}{\frac{\pi}{6} d_m^3} \quad (6)$$

Here, m_p is the particle mass classified by APM, and d_m is the electrical mobility diameter measured by SMPS. A detailed calculation theory related to APM-SMPS system can be found in [96].

Various factors such as precursor category, carbon number, molecular structure (e.g., branched, linear and cyclic), seed particle concentrations (e.g., ammonium sulfate), gaseous

pollutant concentrations (e.g., HO_x and NO_x), and oxidant concentrations (e.g., OH, NO₃, and O₃) affect SOA yield. A detailed discussion regarding the effects of such factors can be found in Srivastava et al. (2022) [11], Lim et al. (2016) [13], and Carlton et al. (2009) [97]. In addition, a review on the properties of SOAs (optical properties, carbon oxidation state, and physical phase state) can be found in Srivastava et al. (2022) [11].

3.7. SOA Losses on Chamber-Wall (Wall Loss)

The smog reactor wall generates static electricity, which captures the SOA particles. This phenomenon may have resulted in an underestimation of SOA yield. Previous studies have quantitatively analyzed this phenomenon to understand SOA wall loss [98–101] and have shown that the amount of wall loss varies with particle size [99] and the carbon number of the compound [100]. In addition, the amount of wall loss depends on various factors such as charge distribution, level of turbulence inside the Teflon reactor bag [101], reactor bag size [12], charge-to-mass ratio based on the size of the charged particles [23], precursor VOC concentration, the oxidation rate of participating pollutants, and experiment duration. Chu et al. [12] compiled wall loss rates in some of the previous studies.

To prevent or alleviate wall loss, previous studies have used two approaches. Jorga et al. [27] used an ionizing fan for 15 min before conducting an experiment to clear the charges on the reactor wall to lower the particle loss rate. In their experiments, they demonstrated that using an ionizing fan reduced the wall loss by a factor of four. The other approach involves using large chambers with small surface-area-to-volume ratios to reduce the effect of wall loss.

To compensate for the effect of wall loss, researchers first calculated the wall loss coefficient based on the decay behavior of SOA concentration and applied this coefficient to correct for the effect of particle wall loss in SOA formation. To do so, previous researchers used number-averaged, volume-averaged, and size-dependent methods. Carter et al. [20] used the number-averaged method, in which they calculated the wall loss rate based on the total aerosol number concentration. Pathak et al. [21] used the volume-averaged method, in which they obtained the loss rate based on the total aerosol volume concentration. Loza et al. [22] and Nah et al. [23] used the size-dependent method, where wall loss coefficients were determined for each particle size bin. They used these coefficients to correct for the wall loss effect in SOA formation more accurately.

The method for obtaining the wall loss coefficient is based on the following particle number or mass balance equations [101],

$$\frac{d}{dt}[C_{sus}] = -k_w C_{sus} + \dot{p}_{sus} \quad (7)$$

$$\frac{d}{dt}[C_{wall}] = k_w C_{sus} + \dot{p}_{wall} \quad (8)$$

where C_{sus} is the number or mass concentration of the suspended particle in the chamber, k_w is the wall loss constant, \dot{p}_{sus} is the rate of production the SOA, C_{wall} is the particle number or mass concentration on the wall, and \dot{p}_{wall} is the loss rate of the condensable vapors to the wall. The wall loss constant (k_w) can be obtained by using a discrete general dynamics equation based on the algorithm proposed by Weitkamp [102] or by measuring the decay rate of the particle number or mass concentration when the light sources are turned off. The wall loss constant (k_w) and time series of the measured and uncorrected SOA concentrations (which correspond to C_{sus} in the above equation) can be used to calculate the wall-loss-corrected SOA production rate (\dot{p}_{sus}) based on the method described by Weitkamp et al. [101].

4. Discussion

The SOA yield is the key parameter in atmospheric models for forecasting total SOA mass concentrations [11]. Because the prediction accuracy relies on the accuracy of the SOA

yield data obtained from smog chamber experiments, it is very important to understand the potential sources of uncertainties in SOA studies.

First, the characteristic gap between artificial light and sunlight presents a source of uncertainty for indoor chambers. The photolysis rate of NO_2 , which is typically used as a proxy for light intensity, varied from 0.10/min to 0.40/min in previous studies (see Table 2). The same photolysis rate of NO_2 between artificial light and sunlight is desired for better simulation of the atmospheric environment. In addition, the photolysis rates of different oxidants are sensitive to the different wavelengths of light. This makes it difficult to maintain identical photolysis rates for multiple oxidants, unless the spectral distributions of artificial light and sunlight are identical. Xenon and Argon arc lamps are known to generate radiation with similar spectral distribution to sunlight [29,54]. However, they are not widely used in chamber studies.

Second, the assumption of SOA density contributes to another source of uncertainty in the SOA yield data. The density assumed in previous studies ranged from 1 g/cm^3 to 1.45 g/cm^3 , which is a significant variation. It is desirable to measure the density of the produced SOA using a combination of a particle sizer and AMS.

Third, wall loss contributes to a significant uncertainty in the SOA yield. Although researchers have attempted to minimize the wall loss by building a larger chamber and developed a method to correct the effect, small chambers with a size of less than 10 m^3 are still actively used in SOA studies, and not all chamber studies have applied wall loss correction. In addition, the SOA formation process is typically very complex, and involves various gases, radicals, and particles. Therefore, it is difficult to measure the wall loss rate of all compounds involved.

Fourth, background contaminants often influence the SOA formation result, and they make it more complex to analyze the result. This uncertainty is significant when ambient air, which normally contains highly complex mixtures of VOCs, is used as a background air of the experiment. To eliminate this uncertainty, a chamber cleaning procedure using purified air is needed.

5. Conclusions

This review summarizes smog chamber systems and methodologies used in 65 chamber-based SOA formation studies. Indoor chambers have the advantage of better controllability for simulating meteorological conditions than outdoor chambers do. However, they are typically built smaller than outdoor chambers and face challenges in closely simulating the wavelength spectrum of sunlight.

A typical experimental method and procedure for a chamber study was explained in this review. The procedure involves characterization of lighting, background contaminants, and wall effect, calibration of measurement devices, cleaning and initialization of chamber, atmospheric simulation, and monitoring. After the experiment, researchers calculate the SOA yield and correct for wall loss.

This review also discussed key chamber parameters that influence SOA formation. Such parameters include temperature, humidity, light intensity, background contaminants, and wall effect. Temperature affects the vapor pressure of VOCs, and humidity affects oxidation processes and gas-particle partitioning of VOCs. The intensity and spectrum of artificial light must be similar to those of natural sunlight, and unwanted background contaminants must be removed.

In addition, potential source of uncertainties in SOA formation experiments were summarized. In previous studies, the intensity (photolysis rate of NO_2 was 0.1–0.40/min) and spectral distribution of artificial lights varied, which contributed to uncertainty in the SOA yield calculation. The methodologies for the SOA yield estimation are discussed in detail. A large number of previous studies assumed an aerosol density of $1\text{--}1.45 \text{ g/cm}^3$ to convert the measured particle size distribution into mass distribution. This is another important source of uncertainty, and it is desirable to avoid assuming aerosol density, but instead measure it using a particle sizer and AMS in future studies. The effect of SOA losses

on the chamber and reactor walls was mitigated using an ionizing fan or corrected based on the particle mass balance equations and the wall loss constant. Wall loss is the third source of uncertainty that must be corrected for all compounds involved in the formation process. Last source of uncertainty may be provided by background contaminants. Elimination or through characterization of the contaminants is necessary to reduce this uncertainty.

Author Contributions: Formal analysis, Methodology, Investigation, Writing—original draft, H.K.; Formal analysis, Methodology, Investigation, Writing—original draft, D.K.; Investigation, Writing—original draft, H.Y.J.; Conceptualization, methodology, J.J.; Conceptualization, Methodology, Investigation, Formal analysis, Visualization, Writing—Review & Editing, Funding acquisition, J.Y.L. All authors have read and agreed to the published version of the manuscript.

Funding: This study was supported by the National Research Foundation of Korea (grant number NRF-2021R1C1C1013350) and by the FRIEND (Fine Particle Research Initiative in East Asia Considering National Differences) Project through the National Research Foundation of Korea (NRF) funded by the Ministry of Science and ICT (grant number NRF-2023M3G1A1090660).

Institutional Review Board Statement: Not applicable.

Informed Consent Statement: Not applicable.

Data Availability Statement: No new data were created or analyzed in this study. Data sharing is not applicable to this article.

Conflicts of Interest: The authors declare no conflict of interest.

References

1. Abaje, I.B.; Bello, Y.; Ahmad, S.A. A review of air quality and concentrations of air pollutants in Nigeria. *J. Appl. Sci. Environ. Manag.* **2020**, *24*, 373–379. [\[CrossRef\]](#)
2. Mitchell, J.F.B.; Johns, T.C.; Gregory, J.M.; Tett, S.F.B. Climate response to increasing levels of greenhouse gases and sulphate aerosols. *Nature* **1995**, *376*, 501–504. [\[CrossRef\]](#)
3. Yang, F.; Tan, J.; Zhao, Q.; Du, Z.; He, K.; Ma, Y.; Duan, F.; Chen, G.; Zhao, Q. Characteristics of PM_{2.5} speciation in representative megacities and across China. *Atmos. Chem. Phys.* **2011**, *11*, 5207–5219. [\[CrossRef\]](#)
4. Intergovernmental Panel on Climate Change (IPCC). *The Physical Science Basis: Contribution of Working Group I to the Sixth Assessment Report of the Intergovernmental Panel on Climate Change, Climate Change*; Cambridge University Press: Cambridge, UK; New York, NY, USA, 2021; p. 2391. [\[CrossRef\]](#)
5. Liu, Q.; Gao, Y.; Huang, W.; Ling, Z.; Wang, Z.; Wang, X. Carbonyl compounds in the atmosphere: A review of abundance, source and their contributions to O₃ and SOA formation. *Atmos. Res.* **2022**, *274*, 106184. [\[CrossRef\]](#)
6. Pope, C.A., III; Dockery, D.W. Health effects of fine particulate air pollution: Lines that connect. *J. Air Waste Manag. Assoc.* **2006**, *56*, 709–742. [\[CrossRef\]](#)
7. Shiraiwa, M.; Ueda, K.; Pozzer, A.; Lammel, G.; Kampf, C.J.; Fushimi, A.; Enami, S.; Arangio, A.M.; Fröhlich-Nowoisky, J.; Fujitani, Y.; et al. Aerosol health effects from molecular to global scales. *Environ. Sci. Technol.* **2017**, *51*, 13545–13567. [\[CrossRef\]](#)
8. Kanakidou, M.; Seinfeld, J.H.; Pandis, S.N.; Barnes, I.; Dentener, F.J.; Facchini, M.C.; Van Dingenen, R.; Ervens, B.; Nenes, A.; Nielsen, C.J.; et al. Organic aerosol and global climate modelling: A review. *Atmos. Chem. Phys.* **2005**, *5*, 1053–1123. [\[CrossRef\]](#)
9. Jathar, S.H.; Gordon, T.D.; Hennigan, C.J.; Pye, H.O.; Pouliot, G.; Adams, P.J.; Donahue, N.M.; Robinson, A.L. Unspeciated organic emissions from combustion sources and their influence on the secondary organic aerosol budget in the United States. *Proc. Natl Acad. Sci. USA* **2014**, *111*, 10473–10478. [\[CrossRef\]](#)
10. Zhang, Q.; Jimenez, J.L.; Canagaratna, M.R.; Allan, J.D.; Coe, H.; Ulbrich, I.; Alfarra, M.R.; Takami, A.; Middlebrook, A.M.; Sun, Y.L.; et al. Ubiquity and dominance of oxygenated species in organic aerosols in anthropogenically-influenced Northern Hemisphere midlatitudes. *Geophys. Res. Lett.* **2007**, *34*, L13801. [\[CrossRef\]](#)
11. Srivastava, D.; Vu, T.V.; Tong, S.; Shi, Z.; Harrison, R.M. Formation of secondary organic aerosols from anthropogenic precursors in laboratory studies. *npj Clim. Atmos. Sci.* **2022**, *5*, 22. [\[CrossRef\]](#)
12. Chu, B.; Chen, T.; Liu, Y.; Ma, Q.; Mu, Y.; Wang, Y.; Ma, J.; Zhang, P.; Liu, J.; Liu, C.; et al. Application of smog chambers in atmospheric process studies. *Natl. Sci. Rev.* **2022**, *9*, nwab103. [\[CrossRef\]](#)
13. Lim, Y.B.; Lee, S.B.; Kim, H.; Kim, J.Y.; Bae, G.N. Review of recent smog chamber studies for secondary organic aerosol. *J. Korean Soc. Atmos. Environ.* **2016**, *32*, 131–157. [\[CrossRef\]](#)
14. Brune, W.H. The Chamber Wall Index for Gas–Wall Interactions in Atmospheric Environmental Enclosures. *Environ. Sci. Technol.* **2019**, *53*, 3645–3652. [\[CrossRef\]](#)
15. Becker, K.H. *The European Photoreactor EUPHORE: Design and Technical Development of the European Photoreactor and First Experimental Results: Final Report of the EC-Project: Contract EV5V-CT92-0059: Funding Period, January 1993–December 1995*; Institute of Physical Chemistry: Warsaw, Poland, 1996.

16. Rohrer, F.; Bohn, B.; Brauers, T.; Brüning, D.; Johnen, F.J.; Wahner, A.; Kleffmann, J. Characterisation of the photolytic HONO source in the atmosphere simulation chamber SAPHIR. *Atmos. Chem. Phys.* **2005**, *5*, 2189–2201. [[CrossRef](#)]
17. Ren, Y.; Grosselin, B.; Daële, V.; Mellouki, A. Investigation of the reaction of ozone with isoprene, methacrolein and methyl vinyl ketone using the HELIOS chamber. *Faraday Discuss.* **2017**, *200*, 289–311. [[CrossRef](#)]
18. Fisseha, R.; Dommen, J.; Sax, M.; Paulsen, D.; Kalberer, M.; Maurer, R.; Höfler, F.; Weingartner, E.; Baltensperger, U. Identification of organic acids in secondary organic aerosol and the corresponding gas phase from chamber experiments. *Anal. Chem.* **2004**, *76*, 6535–6540. [[CrossRef](#)]
19. Bahreini, R.; Keywood, M.D.; Ng, N.L.; Varutbangkul, V.; Gao, S.; Flagan, R.C.; Seinfeld, J.H.; Worsnop, D.R.; Jimenez, J.L. Measurements of secondary organic aerosol from oxidation of cycloalkenes, terpenes, and m-xylene using an Aerodyne aerosol mass spectrometer. *Environ. Sci. Technol.* **2005**, *39*, 5674–5688. [[CrossRef](#)]
20. Carter, W.P.; Cockeriii, D.R., III; Fitz, D.R.; Malkina, I.L.; Bumiller, K.; Sauer, C.G.; Pisano, J.; Bufalino, C.; Song, C. A new environmental chamber for evaluation of gas-phase chemical mechanisms and secondary aerosol formation. *Atmos. Environ.* **2005**, *39*, 7768–7788. [[CrossRef](#)]
21. Pathak, R.K.; Stanier, C.O.; Donahue, N.M.; Pandis, S.N. Ozonolysis of alpha-pinene at atmospherically relevant concentrations: Temperature dependence of aerosol mass fractions (yields). *J. Geophys. Res.* **2007**, *112*, D03201. [[CrossRef](#)]
22. Loza, C.L.; Chhabra, P.S.; Yee, L.D.; Craven, J.S.; Flagan, R.C.; Seinfeld, J.H. Chemical aging of m-xylene secondary organic aerosol: Laboratory chamber study. *Atmos. Chem. Phys.* **2012**, *12*, 151–167. [[CrossRef](#)]
23. Nah, T.; McVay, R.C.; Zhang, X.; Boyd, C.M.; Seinfeld, J.H.; Ng, N.L. Influence of seed aerosol surface area and oxidation rate on vapor wall deposition and SOA mass yields: A case study with α -pinene ozonolysis. *Atmos. Chem. Phys.* **2016**, *16*, 9361–9379. [[CrossRef](#)]
24. Seinfeld, J.H.; Kleindienst, T.E.; Edney, E.O.; Cohen, J.B. Aerosol growth in a steady-state, continuous flow chamber: Application to studies of secondary aerosol formation. *Aerosol Sci. Technol.* **2003**, *37*, 728–734. [[CrossRef](#)]
25. Lee, A.; Goldstein, A.H.; Kroll, J.H.; Ng, N.L.; Varutbangkul, V.; Flagan, R.C.; Seinfeld, J.H. Gas-phase products and secondary aerosol yields from the photooxidation of 16 different terpenes. *J. Geophys. Res.* **2006**, *111*, D17. [[CrossRef](#)]
26. Murphy, S.M.; Sorooshian, A.; Kroll, J.H.; Ng, N.L.; Chhabra, P.; Tong, C.; Surratt, J.D.; Knipping, E.; Flagan, R.C.; Seinfeld, J.H. Secondary aerosol formation from atmospheric reactions of aliphatic amines. *Atmos. Chem. Phys.* **2007**, *7*, 2313–2337. [[CrossRef](#)]
27. Jorga, S.D.; Kaltsonoudis, C.; Liangou, A.; Pandis, S.N. Measurement of formation rates of secondary aerosol in the ambient urban atmosphere using a dual smog chamber system. *Environ. Sci. Technol.* **2020**, *54*, 1336–1343. [[CrossRef](#)]
28. Boyd, C.M.; Sanchez, J.; Xu, L.; Eugene, A.J.; Nah, T.; Tuet, W.Y.; Guzman, M.I.; Ng, N.L.; Ng, N.L. Secondary organic aerosol formation from the β -pinene+ NO₃ system: Effect of humidity and peroxy radical fate. *Atmos. Chem. Phys.* **2015**, *15*, 7497–7522. [[CrossRef](#)]
29. Nah, T.; McVay, R.C.; Pierce, J.R.; Seinfeld, J.H.; Ng, N.L. Constraining uncertainties in particle-wall deposition correction during SOA formation in chamber experiments. *Atmos. Chem. Phys.* **2017**, *17*, 2297–2310. [[CrossRef](#)]
30. Kleindienst, T.E.; Jaoui, M.; Lewandowski, M.; Offenber, J.H.; Lewis, C.W.; Bhawe, P.V.; Edney, E.O. Estimates of the contributions of biogenic and anthropogenic hydrocarbons to secondary organic aerosol at a southeastern US location. *Atmos. Environ.* **2007**, *41*, 8288–8300. [[CrossRef](#)]
31. Al-Naiema, I.M.; Offenber, J.H.; Madler, C.J.; Lewandowski, M.; Kettler, J.; Fang, T.; Stone, E.A. Secondary organic aerosols from aromatic hydrocarbons and their contribution to fine particulate matter in Atlanta, Georgia. *Atmos. Environ.* **2020**, *223*, 117227. [[CrossRef](#)]
32. Hastings, W.P.; Koehler, C.A.; Bailey, E.L.; De Haan, D.O. Secondary organic aerosol formation by glyoxal hydration and oligomer formation: Humidity effects and equilibrium shifts during analysis. *Environ. Sci. Technol.* **2005**, *39*, 8728–8735. [[CrossRef](#)]
33. Na, K.; Song, C.; Cockeriii, D.R. Formation of secondary organic aerosol from the reaction of styrene with ozone in the presence and absence of ammonia and water. *Atmos. Environ.* **2006**, *40*, 1889–1900. [[CrossRef](#)]
34. Vu, D.; Roth, P.; Berte, T.; Yang, J.; Cocker, D.; Durbin, T.D.; Karavalakis, G.; Asa-Awuku, A. Using a new Mobile Atmospheric Chamber (Mach) to investigate the formation of secondary aerosols from mobile sources: The case of gasoline direct injection vehicles. *J. Aerosol Sci.* **2019**, *133*, 1–11. [[CrossRef](#)]
35. Docherty, K.S.; Wu, W.; Lim, Y.B.; Ziemann, P.J. Contributions of organic peroxides to secondary aerosol formed from reactions of monoterpenes with O₃. *Environ. Sci. Technol.* **2005**, *39*, 4049–4059. [[CrossRef](#)] [[PubMed](#)]
36. Song, C.; Na, K.; Cocker, D.R. Impact of the hydrocarbon to NO_x ratio on secondary organic aerosol formation. *Environ. Sci. Technol.* **2005**, *39*, 3143–3149. [[CrossRef](#)]
37. Jahn, L.G.; Wang, D.S.; Dhulipala, S.V.; Ruiz, L.H. Gas-Phase Chlorine Radical Oxidation of Alkanes: Effects of Structural Branching, NO_x, and Relative Humidity Observed during Environmental Chamber Experiments. *J. Phys. Chem. A* **2021**, *125*, 7303–7317. [[CrossRef](#)] [[PubMed](#)]
38. Cai, X.; Ziemba, L.D.; Griffin, R.J. Secondary aerosol formation from the oxidation of toluene by chlorine atoms. *Atmos. Environ.* **2008**, *42*, 7348–7359. [[CrossRef](#)]
39. Schuetzle, D.; Rasmussen, R.A. The molecular composition of secondary aerosol particles formed from terpenes. *J. Air Pollut. Control Assoc.* **1978**, *28*, 236–240. [[CrossRef](#)]
40. Bejan, I.G.; Olariu, R.I.; Wiesen, P. Secondary organic aerosol formation from nitrophenols photolysis under atmospheric conditions. *Atmosphere* **2020**, *11*, 1346. [[CrossRef](#)]

41. Pullinen, I.; Schmitt, S.; Kang, S.; Sarrafzadeh, M.; Schlag, P.; Andres, S.; Kleist, E.; Mentel, T.F.; Rohrer, F.; Kiendler-Scharr, A. Impact of NO_x on secondary organic aerosol (SOA) formation from α -pinene and β -pinene photooxidation: The role of highly oxygenated organic nitrates. *Atmos. Chem. Phys.* **2020**, *20*, 10125–10147. [[CrossRef](#)]
42. Böge, O.; Mutzel, A.; Iinuma, Y.; Yli-Pirilä, P.; Kahnt, A.; Joutsensaari, J.; Herrmann, H. Gas-phase products and secondary organic aerosol formation from the ozonolysis and photooxidation of myrcene. *Atmos. Environ.* **2013**, *79*, 553–560. [[CrossRef](#)]
43. Gatzsche, K.; Iinuma, Y.; Tilgner, A.; Mutzel, A.; Berndt, T.; Wolke, R. Kinetic modeling studies of SOA formation from α -pinene ozonolysis. *Atmos. Chem. Phys.* **2017**, *17*, 13187–13211. [[CrossRef](#)]
44. Kamm, S.; Mohler, O.; Naumann, K.H.; Saathoff, H.; Schurath, U. The heterogeneous reaction of ozone with soot aerosol. *Atmos. Environ.* **1999**, *33*, 4651–4661. [[CrossRef](#)]
45. Lamkaddam, H.; Gratien, A.; Pangui, E.; Cazaunau, M.; Picquet-Varrault, B.; Doussin, J.F. High-NO_x photooxidation of n-dodecane: Temperature dependence of SOA formation. *Environ. Sci. Technol.* **2017**, *51*, 192–201. [[CrossRef](#)] [[PubMed](#)]
46. Chiappini, L.; Perraudin, E.; Maurin, N.; Picquet-Varrault, B.; Zheng, W.; Marchand, N.; Temime-Roussel, B.; Monod, A.; Le Person, A.; Bernard, F.; et al. Organic Aerosol Formation from Aromatic Alkene Ozonolysis: Influence of the Precursor Structure on Yield, Chemical Composition, and Mechanism. *J. Phys. Chem. A* **2019**, *123*, 1469–1484. [[CrossRef](#)] [[PubMed](#)]
47. Henry, F.; Coeur-Tourneur, C.; Ledoux, F.; Tomas, A.; Menu, D. Secondary organic aerosol formation from the gas phase reaction of hydroxyl radicals with m-, o- and p-cresol. *Atmos. Environ.* **2008**, *42*, 3035–3045. [[CrossRef](#)]
48. Du, M.; Voliotis, A.; Shao, Y.; Wang, Y.; Bannan, T.J.; Pereira, K.L.; Hamilton, J.F.; Percival, C.J.; Alfarra, M.R.; McFiggans, G. Combined application of online FIGAERO-CIMS and offline LC-Orbitrap mass spectrometry (MS) to characterize the chemical composition of secondary organic aerosol (SOA) in smog chamber studies. *Atmos. Meas. Tech.* **2022**, *15*, 4385–4406. [[CrossRef](#)]
49. Wang, Y.; Voliotis, A.; Hu, D.; Shao, Y.; Du, M.; Chen, Y.; Kleinheins, J.; Marcolli, C.; Alfarra, M.R.; McFiggans, G. On the evolution of sub- and super-saturated water uptake of secondary organic aerosol in chamber experiments from mixed precursors. *Atmos. Chem. Phys.* **2022**, *22*, 4149–4166. [[CrossRef](#)]
50. Glowacki, D.; Goddard, A.; Hemavibool, K.; Malkin, T.; Commane, R.; Anderson, F.; Bloss, W.; Heard, D.; Ingham, T.; Pilling, M.; et al. Design of and initial results from a highly instrumented reactor for atmospheric chemistry (HIRAC). *Atmos. Chem. Phys.* **2007**, *7*, 5371–5390. [[CrossRef](#)]
51. Massabó, D.; Danelli, S.G.; Brotto, P.; Comite, A.; Costa, C.; Di Cesare, A.; Doussin, J.F.; Ferraro, F.; Formenti, P.; Gatta, E.; et al. ChAMBR: A new atmospheric simulation chamber for aerosol modelling and bio-aerosol research. *Atmos. Meas. Tech.* **2018**, *11*, 5885–5900. [[CrossRef](#)]
52. Kristensen, K.; Jensen, L.N.; Quéléver, L.L.; Christiansen, S.; Rosati, B.; Elm, J.; Teiwes, R.; Pedersen, H.B.; Glasius, M.; Bilde, M.; et al. The Aarhus Chamber Campaign on Highly Oxygenated Organic Molecules and Aerosols (ACCHA): Particle formation, organic acids, and dimer esters from α -pinene ozonolysis at different temperatures. *Atmos. Chem. Phys.* **2020**, *20*, 12549–12567. [[CrossRef](#)]
53. Hartikainen, A.; Yli-Pirilä, P.; Tiitta, P.; Leskinen, A.; Kortelainen, M.; Orasche, J.; Schnelle-Kreis, J.; Lehtinen, K.E.J.; Zimmermann, R.; Sippula, O.; et al. Volatile organic compounds from logwood combustion: Emissions and transformation under dark and photochemical aging conditions in a smog chamber. *Environ. Sci. Technol.* **2018**, *52*, 4979–4988. [[CrossRef](#)]
54. Nordin, E.Z.; Eriksson, A.C.; Roldin, P.; Nilsson, P.T.; Carlsson, J.E.; Kajos, M.K.; Hellén, H.; Wittbom, C.; Rissler, J.; Pagels, J.H.; et al. Secondary organic aerosol formation from idling gasoline passenger vehicle emissions investigated in a smog chamber. *Atmos. Chem. Phys.* **2013**, *13*, 6101–6116. [[CrossRef](#)]
55. Keller, A.; Burtscher, H. A continuous photo-oxidation flow reactor for a defined measurement of the SOA formation potential of wood burning emissions. *J. Aerosol Sci.* **2012**, *49*, 9–20. [[CrossRef](#)]
56. Stefanelli, G.; Jiang, J.; Bertrand, A.; Bruns, E.A.; Pieber, S.M.; Baltensperger, U.; Marchand, N.; Aksoyoglu, S.; Prévôt, A.S.H.; El Haddad, I.; et al. Secondary organic aerosol formation from smoldering and flaming combustion of biomass: A box model parametrization based on volatility basis set. *Atmos. Chem. Phys.* **2019**, *19*, 11461–11484. [[CrossRef](#)]
57. Paulsen, D.; Dommen, J.; Kalberer, M.; Prévôt, A.S.; Richter, R.; Sax, M.; Steinbacher, M.; Weingartner, E.; Baltensperger, U. Secondary organic aerosol formation by irradiation of 1,3,5-trimethylbenzene-NO_x-H₂O in a new reaction chamber for atmospheric chemistry and physics. *Environ. Sci. Technol.* **2005**, *39*, 2668–2678. [[CrossRef](#)] [[PubMed](#)]
58. Ma, W.; Liu, Y.; Zhang, Y.; Feng, Z.; Zhan, J.; Hua, C.; Ma, L.; Guo, Y.; Zhang, Y.; Zhou, W.; et al. A new type of quartz smog chamber: Design and characterization. *Environ. Sci. Technol.* **2022**, *56*, 2181–2190. [[CrossRef](#)]
59. Deng, W.; Liu, T.; Zhang, Y.; Situ, S.; Hu, Q.; He, Q.; Zhang, Z.; Lü, S.; Bi, X.; Wang, X.; et al. Secondary organic aerosol formation from photo-oxidation of toluene with NO_x and SO₂: Chamber simulation with purified air versus urban ambient air as matrix. *Atmos. Environ.* **2017**, *150*, 67–76. [[CrossRef](#)]
60. Deng, W.; Fang, Z.; Wang, Z.; Zhu, M.; Zhang, Y.; Tang, M.; Song, W.; Lowther, S.; Huang, Z.; Jones, K.; et al. Primary emissions and secondary organic aerosol formation from in-use diesel vehicle exhaust: Comparison between idling and cruise mode. *Sci. Total Environ.* **2020**, *699*, 134357. [[CrossRef](#)]
61. Wang, S.; Tsona, N.T.; Du, L. Effect of NO_x on secondary organic aerosol formation from the photochemical transformation of allyl acetate. *Atmos. Environ.* **2021**, *255*, 118426. [[CrossRef](#)]
62. Qi, X.; Zhu, S.; Zhu, C.; Hu, J.; Lou, S.; Xu, L.; Dong, J.; Cheng, P. Smog chamber study of the effects of NO_x and NH₃ on the formation of secondary organic aerosols and optical properties from photo-oxidation of toluene. *Sci. Total Environ.* **2020**, *727*, 138632. [[CrossRef](#)]

63. Chen, L.; Bao, Z.; Wu, X.; Li, K.; Han, L.; Zhao, X.; Zhang, X.; Wang, Z.; Azzi, M.; Cen, K. The effects of humidity and ammonia on the chemical composition of secondary aerosols from toluene/NO_x photo-oxidation. *Sci. Total Environ.* **2020**, *728*, 138671. [[CrossRef](#)] [[PubMed](#)]
64. Babar, Z.B.; Park, J.H.; Kang, J.; Lim, H.J. Characterization of a smog chamber for studying formation and physicochemical properties of secondary organic aerosol. *Aerosol Air Qual. Res.* **2016**, *16*, 3102–3113. [[CrossRef](#)]
65. Pandis, S.N.; Paulson, S.E.; Seinfeld, J.H.; Flagan, R.C. Aerosol formation in the photooxidation of isoprene and β -pinene. *Atmos. Environ. A Gen. Top.* **1991**, *25*, 997–1008. [[CrossRef](#)]
66. Odum, J.R.; Jungkamp, T.P.W.; Griffin, R.J.; Flagan, R.C.; Seinfeld, J.H. The atmospheric aerosol-forming potential of whole gasoline vapor. *Science* **1997**, *276*, 96–99. [[CrossRef](#)] [[PubMed](#)]
67. Yu, Z.; Jang, M.; Zhang, T.; Madhu, A.; Han, S. Simulation of monoterpene SOA formation by multiphase reactions using explicit mechanisms. *ACS Earth Space Chem.* **2021**, *5*, 1455–1467. [[CrossRef](#)]
68. Madhu, A.; Jang, M.; Deacon, D. Modeling the influence of chain length on secondary organic aerosol (SOA) formation via multiphase reactions of alkanes. *Atmos. Chem. Phys.* **2023**, *23*, 1661–1675. [[CrossRef](#)]
69. Kamens, R.; Jang, M.; Chien, C.J.; Leach, K. Aerosol formation from the reaction of α -pinene and ozone using a gas-phase kinetics-aerosol partitioning model. *Environ. Sci. Technol.* **1999**, *33*, 1430–1438. [[CrossRef](#)]
70. Jang, M.; Kamens, R.M. Newly characterized products and composition of secondary aerosols from the reaction of α -pinene with ozone. *Atmos. Environ.* **1999**, *33*, 459–474. [[CrossRef](#)]
71. Jang, M.; Kamens, R.M. Characterization of secondary aerosol from the photooxidation of toluene in the presence of NO_x and 1-propene. *Environ. Sci. Technol.* **2001**, *35*, 3626–3639. [[CrossRef](#)]
72. Leungsakul, S.; Jaoui, M.; Kamens, R.M. Kinetic mechanism for predicting secondary organic aerosol formation from the reaction of d-limonene with ozone. *Environ. Sci. Technol.* **2005**, *39*, 9583–9594. [[CrossRef](#)]
73. Zhou, Y.; Zhang, H.; Parikh, H.M.; Chen, E.H.; Rattanavaraha, W.; Rosen, E.P.; Wang, W.; Kamens, R.M. Secondary organic aerosol formation from xylenes and mixtures of toluene and xylenes in an atmospheric urban hydrocarbon mixture: Water and particle seed effects (II). *Atmos. Environ.* **2011**, *45*, 3882–3890. [[CrossRef](#)]
74. Emanuelsson, E.U.; Hallquist, M.; Kristensen, K.; Glasius, M.; Bohn, B.; Fuchs, H.; Kammer, B.; Kiendler-Scharr, A.; Nehr, S.; Mentel, T.F. Formation of anthropogenic secondary organic aerosol (SOA) and its influence on biogenic SOA properties. *Atmos. Chem. Phys.* **2013**, *13*, 2837–2855. [[CrossRef](#)]
75. Brownwood, B.; Turdziladze, A.; Hohaus, T.; Wu, R.; Mentel, T.F.; Carlsson, P.T.; Tsiligiannis, E.; Hallquist, M.; Andres, S.; Fry, J.L.; et al. Gas-particle partitioning and SOA yields of organonitrate products from NO₃-initiated oxidation of isoprene under varied chemical regimes. *ACS Earth Space Chem.* **2021**, *5*, 785–800. [[CrossRef](#)] [[PubMed](#)]
76. Spittler, M.; Barnes, I.; Bejan, I.; Brockmann, K.J.; Benter, T.; Wirtz, K. Reactions of NO₃ radicals with limonene and α -pinene: Product and SOA formation. *Atmos. Environ.* **2006**, *40*, 116–127. [[CrossRef](#)]
77. Couvidat, F.; Vivanco, M.G.; Bessagnet, B. Simulating secondary organic aerosol from anthropogenic and biogenic precursors: Comparison to outdoor chamber experiments, effect of oligomerization on SOA formation and reactive uptake of aldehydes. *Atmos. Chem. Phys.* **2018**, *18*, 15743–15766. [[CrossRef](#)]
78. Li, J.; Li, H.; Wang, X.; Wang, W.; Ge, M.; Zhang, H.; Zhang, X.; Li, K.; Chen, Y.; Wu, Z.; et al. A large-scale outdoor atmospheric simulation smog chamber for studying atmospheric photochemical processes: Characterization and preliminary application. *J. Environ. Sci.* **2021**, *102*, 185–197. [[CrossRef](#)]
79. Behera, S.N.; Sharma, M. Degradation of SO₂, NO₂ and NH₃ leading to formation of secondary inorganic aerosols: An environmental chamber study. *Atmos. Environ.* **2011**, *45*, 4015–4024. [[CrossRef](#)]
80. Miracolo, M.A.; Hennigan, C.J.; Ranjan, M.; Nguyen, N.T.; Gordon, T.D.; Lipsky, E.M.; Presto, A.A.; Donahue, N.M.; Robinson, A.L. Secondary aerosol formation from photochemical aging of aircraft exhaust in a smog chamber. *Atmos. Chem. Phys.* **2011**, *11*, 4135–4147. [[CrossRef](#)]
81. Kaltsonoudis, C.; Jorga, S.D.; Louvaris, E.; Florou, K.; Pandis, S.N. A portable dual-smog-chamber system for atmospheric aerosol field studies. *Atmos. Meas. Tech.* **2019**, *12*, 2733–2743. [[CrossRef](#)]
82. Jorga, S.D.; Florou, K.; Kaltsonoudis, C.; Kodros, J.K.; Vasilakopoulou, C.; Cirtog, M.; Fouqueau, A.; Picquet-Varrault, B.; Nenes, A.; Pandis, S.N. Nighttime chemistry of biomass burning emissions in urban areas: A dual mobile chamber study. *Atmos. Chem. Phys.* **2021**, *21*, 15337–15349. [[CrossRef](#)]
83. Platt, S.M.; El Haddad, I.; Zardini, A.A.; Clairotte, M.; Astorga, C.; Wolf, R.; Slowik, J.G.; Temime-Roussel, B.; Marchand, N.; Prévôt, A.S. Secondary organic aerosol formation from gasoline vehicle emissions in a new mobile environmental reaction chamber. *Atmos. Chem. Phys.* **2013**, *13*, 9141–9158. [[CrossRef](#)]
84. Ezell, M.J.; Johnson, S.N.; Yu, Y.; Perraud, V.; Bruns, E.A.; Alexander, M.L.; Zelenyuk, A.; Dabdub, D.; Finlayson-Pitts, B.J. A new aerosol flow system for photochemical and thermal studies of tropospheric aerosols. *Aerosol Sci. Technol.* **2010**, *44*, 329–338. [[CrossRef](#)]
85. König, U.; Nitschke, M.; Pilz, M.; Simon, F.; Arnhold, C.; Werner, C. Stability and ageing of plasma treated poly(tetrafluoroethylene) surfaces. *Colloids Surf. B Biointerfaces* **2002**, *25*, 313–324. [[CrossRef](#)]
86. Everett, M.L.; Hoflund, G.B. Chemical alteration of poly(tetrafluoroethylene) TFE Teflon induced by exposure to electrons and inert-gas ions. *J. Phys. Chem. B.* **2005**, *109*, 16676–16683. [[CrossRef](#)]

87. Kim, S.R. Surface modification of poly(tetrafluoroethylene) film by chemical etching, plasma, and ion beam treatments. *J. Appl. Polym. Sci.* **2000**, *77*, 1913–1920. [[CrossRef](#)]
88. Von Hessberg, C.; Von Hessberg, P.; Pöschl, U.; Bilde, M.; Nielsen, O.J.; Moortgat, G.K. Temperature and humidity dependence of secondary organic aerosol yield from the ozonolysis of β -pinene. *Atmos. Chem. Phys.* **2009**, *9*, 3583–3599. [[CrossRef](#)]
89. Chou, A.; Li, Z.; Tao, F.M. Density functional studies of the formation of nitrous acid from the reaction of nitrogen dioxide and water vapor. *J. Phys. Chem. A* **1999**, *103*, 7848–7855. [[CrossRef](#)]
90. Babar, Z.B.; Park, J.H.; Lim, H.J. Influence of NH_3 on secondary organic aerosols from the ozonolysis and photooxidation of α -pinene in a flow reactor. *Atmos. Environ.* **2017**, *164*, 71–84. [[CrossRef](#)]
91. Cocker, D.R., III; Clegg, S.L.; Flagan, R.C.; Seinfeld, J.H. The effect of water on gas–particle partitioning of secondary organic aerosol. Part I: α -pinene/ozone system. *Atmos. Environ.* **2001**, *35*, 6049–6072. [[CrossRef](#)]
92. Seinfeld, J.H.; Erdakos, G.B.; Asher, W.E.; Pankow, J.F. Modeling the formation of secondary organic aerosol (SOA): 2. The predicted effects of relative humidity on aerosol formation in the α -pinene-, β -pinene-, sabinene-, Δ^3 -carene-, and cyclohexene-ozone systems. *Environ. Sci. Technol.* **2001**, *35*, 1806–1817. [[CrossRef](#)]
93. Doussin, J.-F.; Fuchs, H.; Kiendler-Scharr, A.; Seakins, P.; Wenger, J. *A Practical Guide to Atmospheric Simulation Chambers*; Springer: Berlin/Heidelberg, Germany, 2023. [[CrossRef](#)]
94. Rodrigue, J.; Dhaniyala, S.; Ranjan, M.; Hopke, P.K. Performance comparison of scanning electrical mobility spectrometers. *Aerosol Sci. Technol.* **2007**, *41*, 360–368. [[CrossRef](#)]
95. DeCarlo, P.F.; Slowik, J.G.; Worsnop, D.R.; Davidovits, P.; Jimenez, J.L. Particle morphology and density characterization by combined mobility and aerodynamic diameter measurements. Part 1: Theory. *Aerosol Sci. Technol.* **2004**, *38*, 1185–1205. [[CrossRef](#)]
96. Malloy, Q.G.J.; Nakao, S.; Qi, L.; Austin, R.; Stothers, C.; Hagino, H.; Cocker, D.R., III. Real-time aerosol density determination utilizing a modified scanning mobility particle sizer—Aerosol particle mass analyzer system. *Aerosol Sci. Technol.* **2009**, *43*, 673–678. [[CrossRef](#)]
97. Carlton, A.G.; Wiedinmyer, C.; Kroll, J.H. A review of Secondary Organic Aerosol (SOA) formation from isoprene. *Atmos. Chem. Phys.* **2009**, *9*, 4987–5005. [[CrossRef](#)]
98. Grosjean, D. Wall loss of gaseous pollutants in outdoor Teflon chambers. *Environ. Sci. Technol.* **1985**, *19*, 1059–1065. [[CrossRef](#)] [[PubMed](#)]
99. McMurry, P.H.; Grosjean, D. Gas and aerosol wall losses in Teflon film smog chambers. *Environ. Sci. Technol.* **1985**, *19*, 1176–1182. [[CrossRef](#)] [[PubMed](#)]
100. Matsunaga, A.; Ziemann, P.J. Gas-wall partitioning of organic compounds in a Teflon film chamber and potential effects on reaction product and aerosol yield measurements. *Aerosol Sci. Technol.* **2010**, *44*, 881–892. [[CrossRef](#)]
101. Weitkamp, E.A.; Sage, A.M.; Pierce, J.R.; Donahue, N.M.; Robinson, A.L. Organic aerosol formation from photochemical oxidation of diesel exhaust in a smog chamber. *Environ. Sci. Technol.* **2007**, *41*, 6969–6975. [[CrossRef](#)]
102. Weitkamp, E.A. Laboratory Studies of Oxidation of Primary Emissions: Oxidation of Organic Molecular Markers and Secondary Organic Aerosol Production. Ph.D. Thesis, Carnegie Mellon University, Pittsburgh, PA, USA, 2007.

Disclaimer/Publisher’s Note: The statements, opinions and data contained in all publications are solely those of the individual author(s) and contributor(s) and not of MDPI and/or the editor(s). MDPI and/or the editor(s) disclaim responsibility for any injury to people or property resulting from any ideas, methods, instructions or products referred to in the content.